

# Optical Engineering

[SPIDigitalLibrary.org/oe](http://SPIDigitalLibrary.org/oe)

## **Design for source-and-detector configuration of a ring-scanning-based near-infrared optical imaging system**

Jhao-Ming Yu  
Min-Cheng Pan  
Min-Chun Pan

# Design for source-and-detector configuration of a ring-scanning-based near-infrared optical imaging system

## Jhao-Ming Yu

National Central University  
Department of Mechanical Engineering  
Taoyuan County 320, Taiwan

## Min-Cheng Pan

Tung-Nan University  
Department of Electronic Engineering  
New Taipei City 222, Taiwan

## Min-Chun Pan

National Central University  
Department of Mechanical Engineering  
Taoyuan County 320, Taiwan  
and  
National Central University  
Graduate Institute of Biomedical Engineering  
Taoyuan County 320, Taiwan  
E-mail: [pan\\_minc@cc.ncu.edu.tw](mailto:pan_minc@cc.ncu.edu.tw)

**Abstract.** The design scheme of the source-and-detector arrangement of a ring-scanning-based near-infrared optical imaging system prior to the mechanical and optical construction is demonstrated. In terms of the effectiveness and efficiency of design, through the computation of image reconstruction for varied imaging configurations, the influences of the source-and-detector arrangement on the resulting images are evaluated and a formula to estimate the scanning time is provided. The basic idea of our design is to divide circular scanning into several zones, each of which includes  $n$  sources and  $l$  detectors; i.e.,  $m$  zones and  $n$  sources along with  $l$  detectors per zone are defined in the design. Comparison is made among different imaging configurations where their contrast-to-noise ratio measures are evaluated and contrast-and-size detail resolution curves are depicted. Results show that the 2Z3S or 3Z3S configuration is the optimal design in terms of the time consumption of a complete scanning and the resolution of reconstructed optical-property images. © 2014 Society of Photo-Optical Instrumentation Engineers (SPIE) [DOI: [10.1117/1.OE.53.1.011002](https://doi.org/10.1117/1.OE.53.1.011002)]

Subject terms: ring-scanning-based near-infrared optical imaging system; contrast-to-noise ratio; contrast-and-size detail.

Paper 130283SS received Feb. 25, 2013; revised manuscript received Jun. 12, 2013; accepted for publication Jul. 1, 2013; published online Aug. 28, 2013.

## 1 Introduction

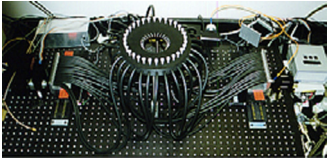
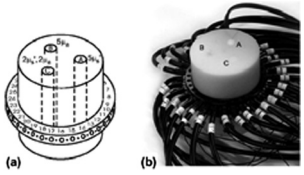
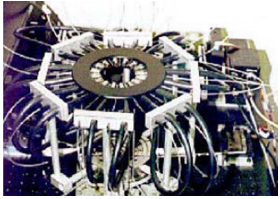


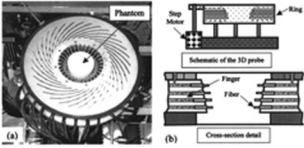
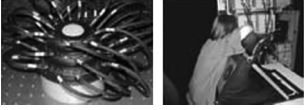

Over the last two decades, there has been increased attention on the use of near-infrared (NIR) diffuse optical tomography (DOT)<sup>1-3</sup> for imaging the interior of biological tissues. Typically, NIR DOT is a noninvasive and nonradioactive functional imaging modality, thereby estimating the NIR absorbing and scattering properties of the tissue, and has the potential to become a useful tool for clinical diagnosis of tumors. Further, it is feasible that utilizing multiple spectra absorption properties is capable of evaluating oxyhemoglobin, deoxyhemoglobin, water, and lipid concentrations in the phantom/breast.

Basically, the source-detector-phantom geometries chosen for many laboratory and clinical NIR imaging studies fall into three general categories, which are delineated here as (1) projection-shadow such as fan-beam tomography, (2) full reflectance-and-transmittance tomography, and (3) subsurface imaging below a boundary. Comparisons have been made among the reconstructed optical-property images produced in the above three different geometries where each of these three were examined in a circular and a flat slab geometry.<sup>4</sup> It was found that preliminary simulations using a mesh of the human brain confirmed that optimal images were produced from circularly symmetric source-detector distributions; furthermore, not only sampling of the whole space but also maximal angular sampling was required for optimal image reconstruction. Therefore, the circular source-and-detector arrangements with full reflectance-and-transmittance tomography are investigated in this paper. In addition, the source-and-detector architecture is designed

to be able to rotate around the circumference of the tested phantom. The advantage of scanning is its flexible sampling to obtain a required maximal resolution rather than a fixed source-and-detector arrangement.

Based on the point view of the source-and-detector allocation in a circular configuration of the NIR DOT imaging system, it can be divided into four general categories that possess the following characteristics: (1) ring- or hemisphere-based distribution and (2) fixed or switching/scanning mechanism. Varied designs are summarized and shown in Table 1. From item 1 to item 10 for the architecture of ring-and-fixed-based distribution, basically, source and detector optical fibers are arranged around the circumference of a cylinder phantom or a breast. A laser diode output is multiplexed through the source fibers by a fiber optic switch and light from the diode laser is transmitted sequentially to source points; all detector fiber bundles are illuminated simultaneously or sequentially by a source excitation. In item 3, the central ring of the interface provides the structural support to allow the fibers to be mechanically configured into variable diameters of 5 to 10 cm; similarly, radially arranged linear translation stages were used to acquire a single coronal tomographic plane through the breast in item 4; in item 5, the diameter of the circular interface of source and detector fiber optics can be changed from 66 to 200 mm by control of stepper motor stages. In item 6, a 16 source excitation by 16 detection combination was used per layer and four layers were acquired at the three-dimensional (3-D) probe by moving four steps up and down. In item 9, a spectrometer-based detection system for continuous wave tomography was operated with a 16 charge-coupled-device-coupled imaging monochromator.

**Table 1** Literature review for varied designs of the measuring module in near-infrared diffuse optical tomography.

Item	Reference number	Measuring architecture	Team	Arrangement <sup>a,b</sup>	cw/FD/TD <sup>c</sup>	Wavelength
1	5		Dartmouth College	16S + 16D → 16S × 16D	FD (100 MHz)	800 nm
2	6		University College London	32S + 32D → 32S × 32D	TD (500 ps)	800 nm
3	7		Dartmouth College	16S + 16D → 16S × 16D	FD (100 MHz)	750, 800 nm
4	8		Dartmouth College	16S + 16D → 16S × 16D	FD (100 MHz)	761, 785, 808, 826 nm
5	9		Dartmouth College	16S + 16D → 16S × 16D	FD (100 MHz)	761, 785, 808, 826 nm
6	10		Clemson University	16S + 16D → 16S × 16D × 4L	cw	785, 808, 830 nm
7	11		University College London	16S + 16D → 16S × 16D	TD	780, 815 nm
8	12, 13		University of California (Irvine)	8S + 8D → 8S × 8D	FD (110 MHz–280 MHz)	665, 785, 800, 830 nm

**Table 1** (Continued).

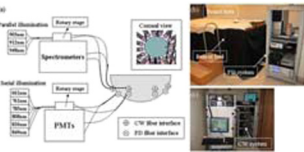
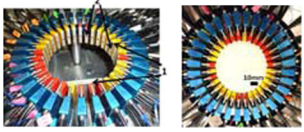
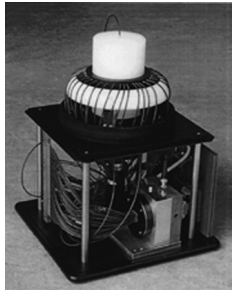
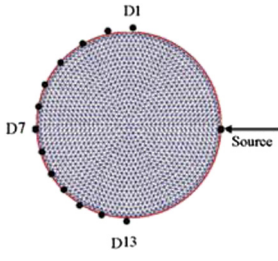
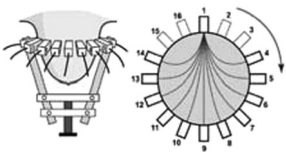
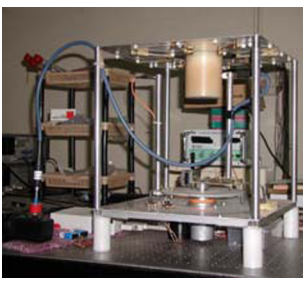

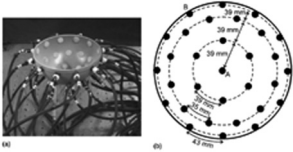
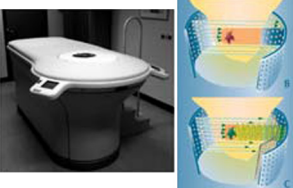

Item	Reference number	Measuring architecture	Team	Arrangement <sup>a,b</sup>	cw/FD/TD <sup>c</sup>	Wavelength
9	14		Dartmouth College	16S + 16D → 16S × 16D	cw and FD	903, 912, 948, 661, 761, 785, 808, 826, 849 nm
10	15		University of Florida	16S + 16D → 16S × 16D	cw	775 nm
11	16		Leiden University	1S + 16D(fan/scanning) → 16S × 16D	TD (160 fs)	780 nm
12	17		Indian Institute of Science	1S + 16D(fan/scanning) → 16S × 16D	cw	
13	18		Rensselaer Polytechnic Institute	16SD → 16S × 11D(fan)	cw	805 nm
14	19		Indian Institute of Science	20SD → 20S × 19D	FD (100 MHz)	785 nm
15	20		Philips, University of Amsterdam	256SD(3 - D) → 256S × 255D	cw	660, 780, 920 nm

Table 1 (Continued).

Item	Reference number	Measuring architecture	Team	Arrangement <sup>a,b</sup>	cw/FD/TD <sup>c</sup>	Wavelength
16	21		University College London	31SD(3 - D) → 31S × 30D	TD	780, 815 nm
17	22		Philips Healthcare	253S + 254D(3 - D) → 253S × 254D	cw	690, 730, 780, 850 nm
18	23, 24		Columbia University, State University of New York	(16S + 16D) × 2(3 - D) → 32S × 64D	cw	765, 808, 827, 805 nm

<sup>a</sup> $nS + lD$  means there are  $n$  sources and  $l$  detectors in the measuring device, thereby leading to the acquired information of an  $nS \times lD$  combination;  $kSD$  indicates there are  $k$  sources and detectors in total as well as excitation and detection can be switched with each other; <sup>b</sup>3-D in parentheses means sources and detectors were distributed over a three-dimensional cup; <sup>c</sup>FD, frequency domain; TD, time domain.

In items 11 to 14, the source and detectors are rotated around the phantom or collocated (items 13 and 14) in a circular plane. The fan-beam optical tomography was setup for experimental trials and the cylindrical phantom was rotated around its axis in item 11; the detectors used the same positions as the sources to collect the light originating from one source at a time where the signals from only the farther part of detectors and other positions were used in the analysis in items 13 and 14, respectively.

From items 15 to 18, the hemispherical cup geometry was developed for breast imaging in order to be able to obtain a 3-D image where optical fibers were mounted on the boundary of the cup and the transmission of the breast was measured over a conical surface. In item 17, sources and detectors were positioned at opposite sides of the breast in transillumination and the cup was filled with a matching fluid that has optical properties approximately equal to those of the average breast for each scan. In the measuring apparatus of item 18, sources and detectors were arranged in a flat geometry beneath the breast, while the other sources and detectors were brought into contact with the top of the breast with several adjustable fingers holding fibers. However, there are no designs for 3-D hemisphere-and-scanning-based configuration to date.

In this study, our aim is to focus on a ring-scanning-based measuring module and apply image reconstruction algorithm (Tikhonov regularization) in the frequency domain (FD) for different imaging configurations to evaluate how the

source-and-detector arrangement affects the resulting image. This ring-scanning-based measuring module of the NIR DOT imaging system is designed as a source-and-detector ring rotating around the circumference of the tested phantom with a high degree of spatial flexibility. Furthermore, the measuring module is operated in the FD to achieve the information of amplitude and phase for reconstructing a better optical-property image quality rather than amplitude used alone. The architecture of this FD imaging system is shown in Fig. 1.

This paper is organized as follows. Section 2 describes the method to design a ring-scanning-based source-and-detector arrangement; in addition, the image reconstruction algorithm used is briefly described. Subsequently, the evaluation method with combining a contrast-and-size detail (CSD) with the contrast-to-noise ratio (CNR) is explained in Sec. 3. Then, a comparison is made among the results achieved from different source-and-detector arrangements and, consequently, an optimal design is suggested in Sec. 4. Finally, concluding remarks are made in Sec. 5.

## 2 Design of a Ring-Scanning-Based Imaging System

### 2.1 Design of Different Ring-Scanning Mechanisms

In this section, we describe the design of a ring scanning mechanism. Compared with the measuring module of a single source and a single detector, a system with several

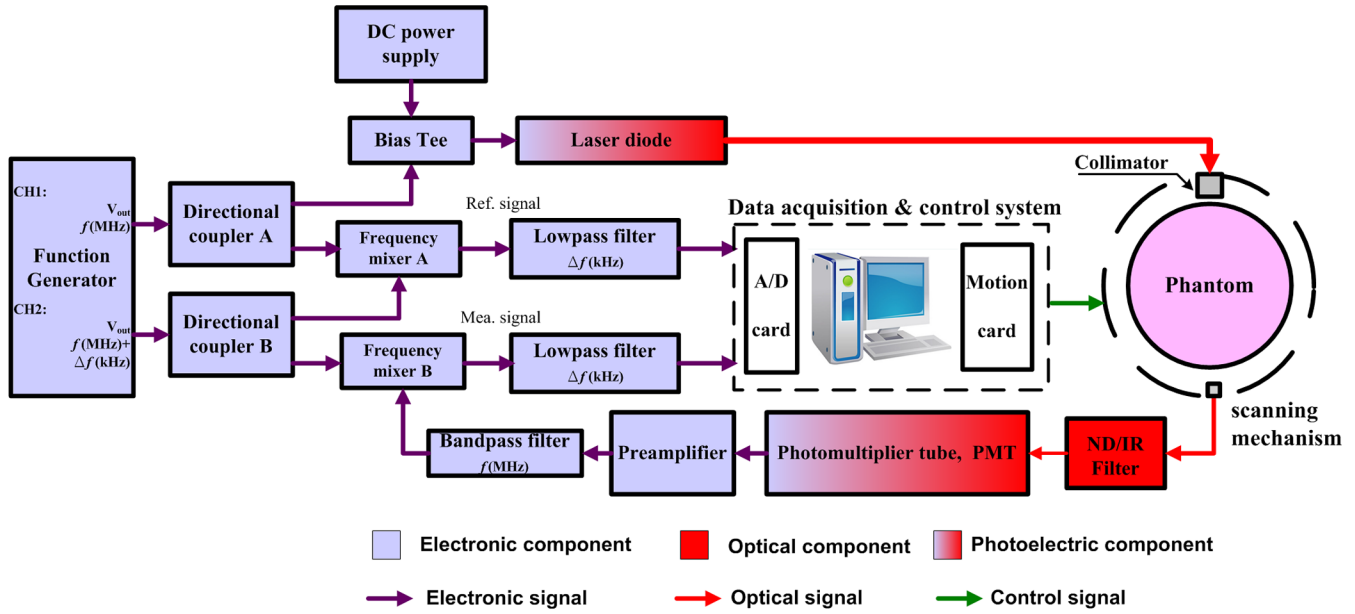


Fig. 1 Architecture of the frequency-domain NIR DOT imaging system.

sources and detectors can reduce the scanning time. Currently, our design is to divide a circular scanning into several zones, each of which includes  $n$  sources and  $l$  detectors; i.e.,  $m$  zones and  $n$  sources along with  $l$  detectors per zone are defined for source-and-detector configurations in the measuring module of the NIR DOT imaging system. Considering the physical dimensions of source and detection fiber heads, 36 sources and detectors in total are adopted, with separation between both heads being 10 deg, and this source-and-detector ring is 100 mm in diameter.

Therefore, a set of design criteria can be concluded as given below in Eqs. (1) to (4).

$$N_{\text{Source}}^Z + N_{\text{Detector}}^Z = \frac{N_{\text{total}}}{N_{\text{Zone}}}, \quad (1)$$

$$\theta_{\text{source/detection}} = \frac{360 \text{ deg}}{N_{\text{total}}}, \quad (2)$$

$$N_{\text{Scanning}} = \frac{N_{\text{Detector}}^Z}{N_{\text{Source}}^Z}, \quad (3)$$

$$\theta_{\text{Rotation}} = \theta_{\text{source/detection}} \times N_{\text{Detector}}^Z, \quad (4)$$

where  $N_{\text{total}}$  is the number of sources and detectors in total, here  $N_{\text{total}}$  is 36,  $N_{\text{zone}}$  is the number of zones,  $\theta_{\text{source/detection}}$  is the distributed angle between the adjacent sources or detections, equal to 10 deg here,  $N_{\text{Source}}^Z$  and  $N_{\text{Detector}}^Z$  are the number of sources and detectors per zone, respectively, and  $N_{\text{Scanning}}$  and  $\theta_{\text{Rotation}}$  are the number of scanning operations and the rotation angle for one cycle of measurement, correspondingly.

In this study, we propose nine configurations of ring scanning, as shown in Table 2, and the varied source-detector-and-zone combinations are also shown in the table. That a ring circumference is divided into one, two, or three zones indicates that the rotation angle ( $\theta_{\text{Rotation}}$ ) of the

whole rotating mechanism is  $\sim 360, 180,$  or  $120$  deg, respectively, and the scanning time of the first one is about three times that of the third one. As can be concluded, there is more detection for one zone than three zones; that is, the less the scanning time and the detection, the more the zones. Furthermore, one, two, or three sources can be placed within each zone; as expected, more sources can reduce scanning time, however, less detection leads to resolution reduction.

For a complete cycle of scanning to acquire information, the total time is termed as the following equation:

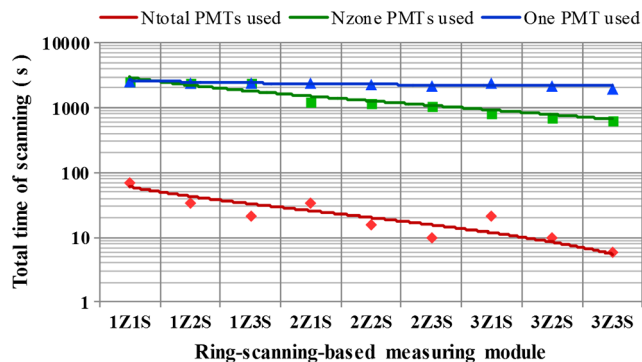
$$\begin{aligned} t_{\text{total}} &= N_{\text{Scanning}} \times t_{\text{Scanning}} + N_{\text{Scanning}} \times N_{\text{Zone}} \times N_{\text{Source}}^Z \\ &\quad \times (t_{\text{excitation}} + N_{\text{Zone}} \times N_{\text{Detector}}^Z \times t_{\text{detection}}) \\ &= \frac{N_{\text{Detector}}^Z}{N_{\text{Source}}^Z} \times t_{\text{Scanning}} + \frac{N_{\text{Detector}}^Z}{N_{\text{Source}}^Z} \times \frac{N_{\text{total}}}{N_{\text{Source}}^Z + N_{\text{Detector}}^Z} \\ &\quad \times N_{\text{Source}}^Z \times (t_{\text{excitation}} + \frac{N_{\text{total}}}{N_{\text{Source}}^Z + N_{\text{Detector}}^Z} \\ &\quad \times N_{\text{Detector}}^Z \times t_{\text{detection}}) = \frac{N_{\text{Detector}}^Z}{N_{\text{Source}}^Z} \times t_{\text{Scanning}} + N_{\text{total}} \\ &\quad \times (t_{\text{excitation}} + \frac{N_{\text{total}}}{N_{\text{Source}}^Z + N_{\text{Detector}}^Z} \times N_{\text{Detector}}^Z \times t_{\text{detection}}) \\ &\approx \frac{N_{\text{Detector}}^Z}{N_{\text{Source}}^Z} \times t_{\text{Scanning}} \text{ (for } N_{\text{total}} \text{ PMTs used)} \\ &\approx \frac{N_{\text{Detector}}^Z}{N_{\text{Source}}^Z} \times t_{\text{Scanning}} + N_{\text{total}} \times N_{\text{Detector}}^Z \\ &\quad \times t_{\text{detection}} \text{ (for } N_{\text{Zone}} \text{ PMTs used)} \\ &\approx \frac{N_{\text{Detector}}^Z}{N_{\text{Source}}^Z} \times t_{\text{Scanning}} + N_{\text{total}} \times \frac{N_{\text{total}}}{N_{\text{Source}}^Z + N_{\text{Detector}}^Z} \\ &\quad \times N_{\text{Detector}}^Z \times t_{\text{detection}} \text{ (for 1 PMT used),} \end{aligned} \quad (5)$$

where  $t_{\text{total}}$  is the total time for a complete scanning,  $t_{\text{Scanning}}$  is the time to rotate the sources and detectors to next stage,

**Table 2** Nine configurations designed for a ring-scanning-based measuring module.

	mZ1S	mZ2S	mZ3S
1Zns	 <p>(1Source + 35Detectors) × 1Zone → 36 Sources × 35 Detectors</p>	 <p>(2Sources + 34Detectors) × 1Zone → 36 Sources × 34 Detectors</p>	 <p>(3Sources + 33Detectors) × 1Zone → 36 Sources × 33 Detectors</p>
2Zns	 <p>(1Source + 17Detectors) × 2Zones → 36 Sources × 34 Detectors</p>	 <p>(2Sources + 16Detectors) × 2Zones → 36 Sources × 32 Detectors</p>	 <p>(3Sources + 15Detectors) × 2Zones → 36 Sources × 30 Detectors</p>
3Zns	 <p>(1Source + 11Detectors) × 3Zones → 36 Sources × 33 Detectors</p>	 <p>(2Sources + 10Detectors) × 3Zones → 36 Sources × 30 Detectors</p>	 <p>(3Sources + 9Detectors) × 3Zones → 36 Sources × 27 Detectors</p>

$t_{\text{detection}}$  is the detection time including a detector switching and acquiring signal. According to our experience, the time of  $t_{\text{scanning}}$  ( $\sim 2$  s),  $t_{\text{detection}}$  ( $\sim 2$  s plus 3.5 ms), and  $t_{\text{excitation}}$  ( $\sim 0.1$  ms) were measured and thus the total time ( $t_{\text{total}}$ ) under varied configurations for one or multiple photomultiplier tubes (PMTs) is plotted as Fig. 2. For example, it takes around 43, 20, and 10 min for  $N_z$  PMTs used under



**Fig. 2** Illustration for the total time of scanning with varied numbers of PMTs.

1Z1S, 2Z2S, and 3Z3S configurations, accordingly, while 43, 40, and 35 min are required, respectively, for one PMT used. Furthermore, if multiple PMTs for all detectors are used, it can allow the measurements from all excitation positions without switching the detection positions frequently, thereby reducing the time required for data acquisition—only 72, 18, and 8 s are required under 1Z1S, 2Z2S, and 3Z3S configurations, correspondingly.

## 2.2 Image Reconstruction Algorithm

In NIR DOT imaging, the fundamental equation governing the propagation of light in biological tissues is approximately described with the diffusion equation to model the optical characteristics of scattering and absorption. The finite element method (FEM)-based image reconstruction in the FD is concluded as the following equations.<sup>25</sup>

As described, the physical process can be described from a diffusion equation.

$$\nabla \cdot D \nabla \Phi(r, \omega) - \left( \mu_a - \frac{i\omega}{c} \right) \Phi(r, \omega) = -S(r, \omega), \quad (6)$$

where  $S(r, \omega)$  and  $\Phi$  denote the source and the radiance, respectively.  $\mu_a$ ,  $c$ , and  $D$  are the absorption coefficient, the wave speed in the medium, and the diffusion coefficient, respectively. Moreover, the diffusion coefficient depends on the reduced scattering coefficient  $\mu'_s$  as  $D = 1/[3(\mu'_s + \mu_a)]$ . For solving Eq. (6), FEM based on the Galerkin weak form of Eq. (6) along with a boundary condition,  $-D\nabla\Phi \cdot \hat{n} = \alpha\Phi$  (flux in fact), is implemented where  $\alpha$  is a determinable coefficient. Following that, using partial differentiation with  $\partial/\partial D$  and  $\partial/\partial\mu_a$ , respectively, we can obtain  $\partial\Phi_b/\partial D_k$  and  $\partial\Phi_b/\partial\mu_{al}$ . Then, applying the Taylor expansion method and ignoring higher-order terms, we obtain

$$J\Delta\chi = \Delta\Phi, \tag{7}$$

where the Jacobian matrix  $J$  denotes  $J(\frac{\partial\Phi_b}{\partial D_k}, \frac{\partial\Phi_b}{\partial\mu_{al}})$ ,  $\Delta\chi$  is  $\Delta\chi(\Delta D_k, \Delta\mu_{al})$ , and  $\Delta\Phi$  is the vector with differences between calculated intensities ( $\Phi_{cal}$ ) and measured intensities ( $\Phi_{meas}$ ). Also,  $D_k$  for  $k = 1, 2, \dots, K$  and  $\mu_{al}$  for  $l = 1, 2, \dots, L$  are the reconstruction parameters for the optical-property profile. Subsequently, Eq. (7) is regularized with Tikhonov regularization to iteratively update the diffusion and absorption coefficients, i.e.,

$$\begin{bmatrix} \Delta\mu_a \\ \Delta D \end{bmatrix} = ([J]^T[J] + \lambda I)^{-1}[J]^T[\Phi^{Meas.} - \Phi^{Cal.}], \tag{8}$$

where  $\lambda$  is a Tikhonov regularization parameter of the Jacobian matrix.

### 3 Evaluation Method

Evaluating a new imaging configuration requires knowledge of the validity of the reconstructed images, and the CNR can be employed to generate contrast-detail curves for determining the system performance and allowing comparison among varied imaging configurations.

CNR is defined as the difference between the region of interest (ROI) and the background region values of the optical properties (i.e., the absorption and reduced scattering coefficients) divided by the averaged optical coefficient variation in the background. Although there is only one choice for the ROI location, there are different choices for the background that can be used for the analysis. In Fig. 3, a schematic diagram is shown for the definition of

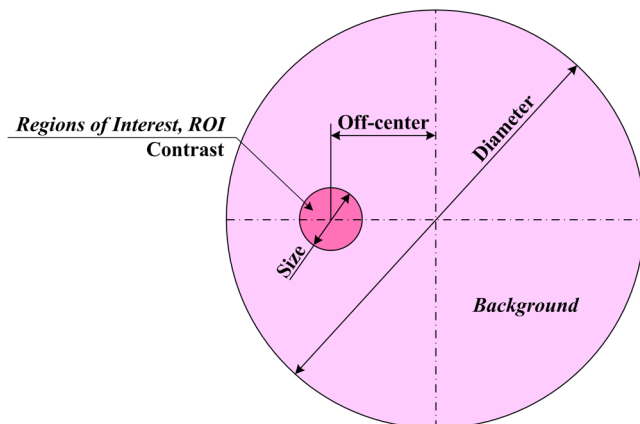


Fig. 3 A schematic diagram for defining CNR.

CNR. One can define the contrast in the reconstructed image as the difference of the mean values in the target and background and include a noise weight into the CNR definition because the background and ROI have different contributions to the whole noise; CNR can be defined as

$$CNR = \frac{\bar{\mu}_{ROI} - \bar{\mu}_{background}}{\sqrt{(w_{ROI} * \sigma_{ROI}^2 + w_{background} * \sigma_{background}^2)/2}}, \tag{9}$$

$$w_x = \frac{AREA_x}{AREA_{ROI} + AREA_{background}},$$

$x = ROI \text{ or } background,$

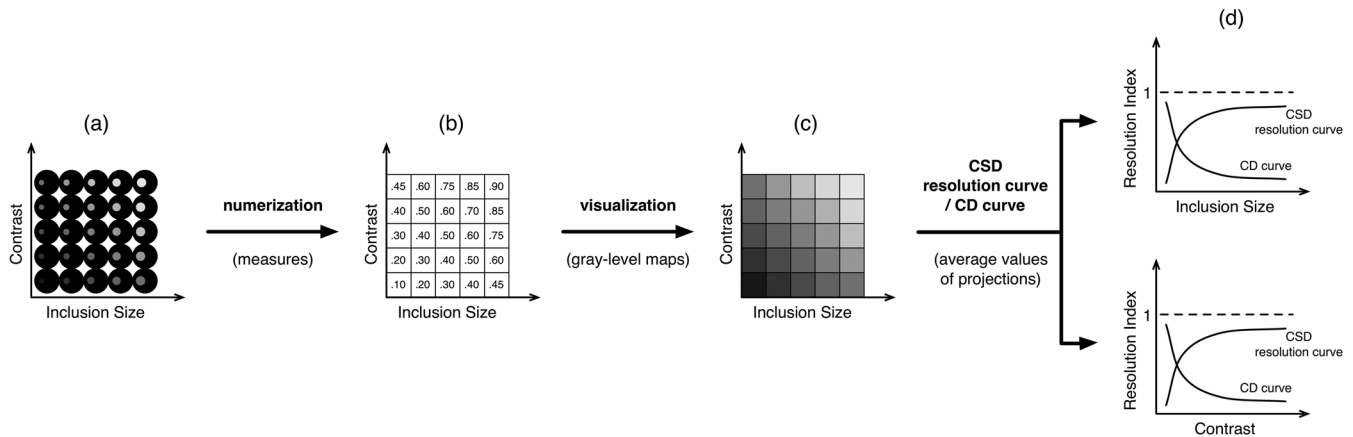
where  $\bar{\mu}_{ROI}$  is the mean of the node values in the target,  $\bar{\mu}_{background}$  is the mean value over the variable background, and  $\sigma_{ROI}$  and  $\sigma_{background}$  are the standard deviations of the collectivities of the target and the background areas, respectively. It is worth mentioning that we chose the fibro-glandular as the background for the magnetic resonance imaging (MRI) in the CNR estimation.

Contrast-detail (CD) analysis<sup>26,27</sup> resulting in the minimum detectable contrast level which has been well accepted in mammography research and quality control, is commonly used to determine the performance of medical imaging systems for assessing the imaging capabilities as well as medical image reconstruction algorithms for evaluating the reconstructing resolution. However, the determination and reproducibility of absolute vanishing detection thresholds for several targets of different contrast by human observers yield a high degree of error. Because of the large total observer error, CD analysis may be impractical in a clinical environment, unless there is access to a team of observers specifically and extensively trained in this task; i.e., the subjective nature of human perception and the variations in the decision threshold pose limits to the minimum image quality variations detectable with reliability. Traditionally, CD curves are derived subjectively by human inspection;<sup>28,29</sup> alternatively, a threshold was used as the measure of detection rather than repeated observers.<sup>30</sup> Given a chosen threshold value of CNR, it is straightforward to calculate the CNR values of reconstructed images and find those images in which objects appear to be detectable.

To overcome the above limitations, the approach used in Ref. 31, which provides a visualization method based on numerical assessment, is utilized for the evaluation of optical-property images of NIR DOT; furthermore, a CSD resolution curve can be plotted by calculating the average value of the projection corresponding to the physical quantity/axis (size or contrast). The schematic diagram of this approach used here is illustrated as Fig. 4.

Therefore, the contrast-and-size map of resolution can be calculated with Eq. (9) for each corresponding image in the map as well as imaged for visualization. Similar to CD curves but not judged under a subjective condition, in the contrast-and-size map of numerical assessment, the average value of the projection, defined as the resolution index, is determined for each size or contrast corresponding to the axis (size or contrast); if this is repeated for all sizes on the axis, a CSD resolution curve corresponding to the size can be plotted, representing the resolution ability of contrasts for all sizes. Furthermore, a CSD resolution can be subtracted from one as a CD curve to correspond to the





**Fig. 4** The schematic diagram of generating a CSD resolution curve. (a) Reconstructing images for a range of inclusion diameters and contrast levels. (b) Calculating the measure, CNR [Eq. (9)], for each reconstruction image in (a). (c) Generating the contrast-and-size map of resolution by using numerical values in (b) as gray-level intensities. (d) Calculating average CNR for each contrast or size, and plotting a CSD resolution or CD curve, respectively.

minimum detectable range of contrasts for all sizes. As well, the same procedure can be done corresponding to the contrast axis.

#### 4 Results and Discussion

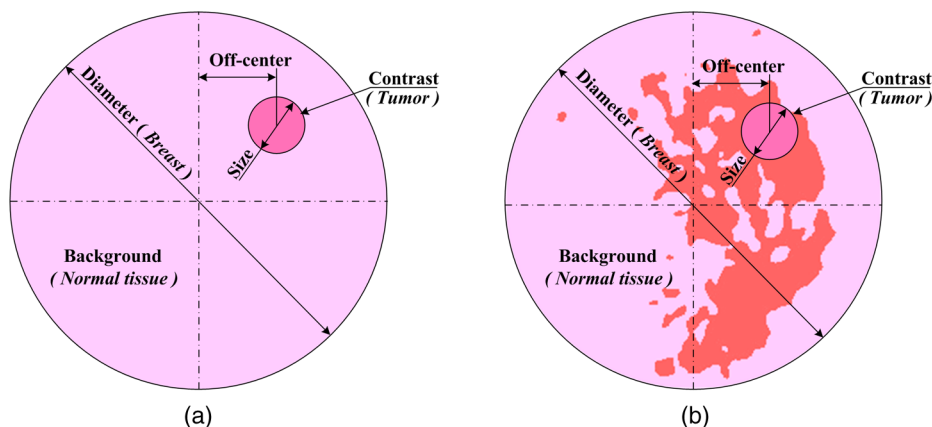
In this section, we evaluate the results obtained from our proposed design of different source-and-detector arrangements and scanning as described in the previous section. For our simulation studies, a breast-like image and an MRI breast image with an added inclusion were used for simulation to evaluate different configurations, as shown in Table 2 and Fig. 5; the tested two-dimensional image is 100 mm in diameter and the background medium has values of  $\mu'_s = 0.6 \text{ mm}^{-1}$  and  $\mu_a = 0.006 \text{ mm}^{-1}$ . Within this field, a circular inclusion with a variable diameter (5, 10, or 15 mm) small region representing a target or tumor area was located 15, 20, or 25 mm away from the center along 45 deg for both images, respectively, depicted in Fig. 5. Specifically, the contrast of the target to background in absorption and reduced scattering at 2.5:1, 3:1, or 4:1 was studied; further, the contrast was 1.5:1 for fibro-glandular to background in the MRI breast image. For the cases of varied contrasts, sizes, and locations of the inclusion, 27 tests (3 contrasts  $\times$  3 sizes  $\times$  3 locations of the inclusion) are computed where an inclusion/tumor is contained against the background. Thus,

243(= 27 cases  $\times$  9 configurations) trials in total were simulated for this research. The modulation frequency was selected to be 100 MHz and 1 KHz was for  $\Delta f$ , and multiple source excitation and detection positions described as in Table 2 were used to simulate the boundary collected information needed in the reconstructions. The computer code used is our self-developed program, NIR.FD\_PC, in Matlab<sup>TM</sup>.

In the following simulations, a fine mesh with 3169 nodes and 6144 triangular elements and a coarse mesh with 1089 nodes and 2048 triangular elements were applied in the forward solver and reconstruction, respectively. In the cases shown here, the regularization parameter was chosen to provide optimal reconstructions through a series of trials, so that the reconstructed images were our best attempt. In the reconstruction, the images were stopped when the changes in optical coefficients in consecutive iterations were below a threshold, which were converged within 10 iterations in a 2.40 GHz dual-core PC with 8 GB memory.

##### 4.1 Results of Application to a Homogenous Background with a Single Inclusion

A breast-like image, a homogenous background image with a single inclusion, was used for simulation and thus 243



**Fig. 5** A schematic diagram of (a) a breast-like image and (b) an MRI breast image with an added inclusion.

reconstructed  $\mu_a$  or  $\mu'_s$  images were generated; however, it will be redundant and burdensome to provide those images here. Therefore, we apply the approach shown in Fig. 4 and the measured CNR to the reconstructed images and then obtain the contrast-and-size map of resolution shown in Figs. 6 and 7 for the reconstructed  $\mu_a$  and  $\mu'_s$  images, respectively.

As can be seen in Fig. 6, the CNR values of the reconstructed  $\mu_a$  images were estimated and ranges were between (0, 10). Basically, the CNR value is increasing from bottom-left part to top-right part; i.e., an inclusion with a larger size and a higher contrast has a higher CNR value than one with a small size or a low contrast. From the map presented here, we can easily but roughly evaluate how good the reconstruction is from its bright or dark appearance rather than judging from the reconstructed images or using CD curves.

For a certain source-and-detector arrangement, there is a better differentiation for those phantom images with an inclusion near the boundary as comparing varied off-centered inclusions of three submaps on each row. Nevertheless, a phenomenon is observed that CNR values of the inclusion (diameter: 15 mm, contrast: 3 or 4, and off-center: 25 mm) shown on the top-right of the submap are not larger/brighter than those with a diameter of 10 mm shown on the top-middle of the submap, implying that a cross-talk exists between high contrast and large size of an inclusion.

As can be seen, only a slight difference is presented in the maps among various arrangements from visual judgment. Thus, further analysis is required with the help of the CSD or CD curve; this will be shown in Sec. 4.3.

For the map of resolution for the reconstructed  $\mu'_s$  images shown in Fig. 7, the CNR values are in the range (0, 5). In Fig. 7, there is a similar trend for CNR values as the map of resolution for the reconstructed  $\mu_a$  images; i.e., there is a high differentiation for a large-size and high-contrast inclusion no matter what arrangement was used. As seen in detail, a cross-talk seems not to appear in  $\mu'_s$  images.

#### 4.2 Results of Application to an MRI Breast Image with a Single Inclusion

To apply these source-and-detector arrangements in a more practical case, an MRI breast image was employed in the diffuse optical imaging (DOI) system to create a synthesized numerical case using one of the nine source-and-detector configurations. As shown in Figs. 8 and 9, the CNR values of the reconstructed  $\mu_a$  and  $\mu'_s$  images vary between (0, 5) and (0, 2.5), respectively, which is lower or darker than the cases described above because of the comparison made between the inclusion and the fibro-glandular, of which the contrast of inclusion-to-fibro-glandular in the MRI breast image is lower than that of inclusion-to-background in the breast-like images. As the inclusion contrast or size increases in Figs. 8 and 9, the submaps show brighter

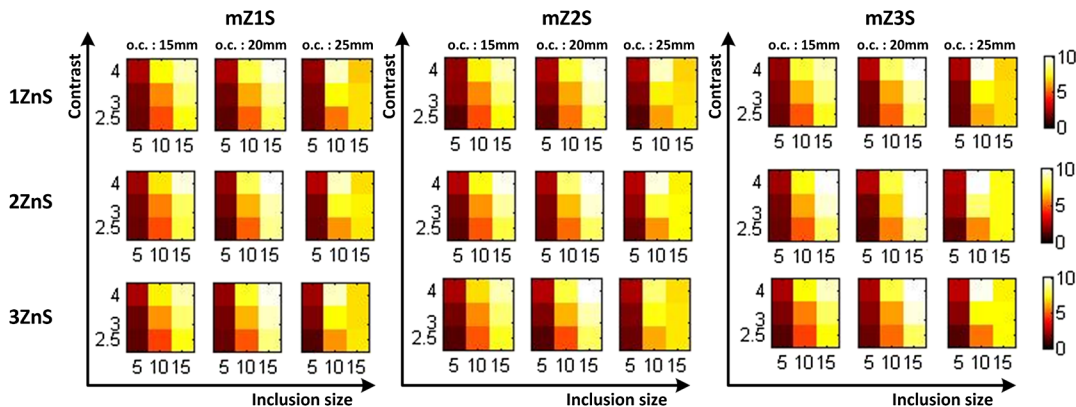


Fig. 6 The contrast-and-size map of resolution by using CNR values as gray-level intensities for the reconstructed absorption-coefficient images of a breast-like image.

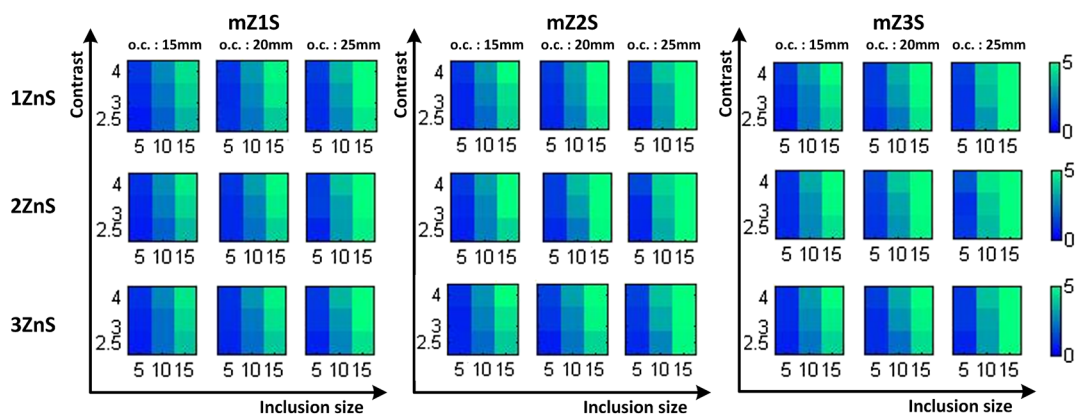
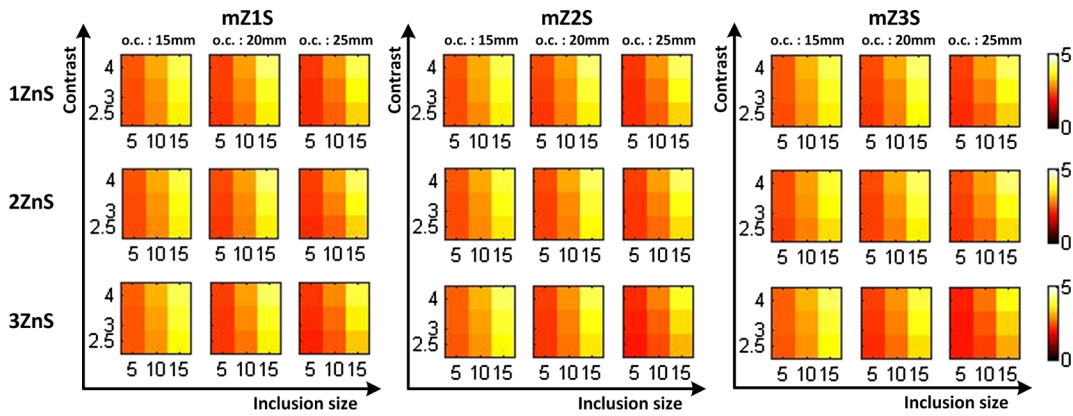


Fig. 7 The contrast-and-size map of resolution by using CNR values as gray-level intensities for the reconstructed reduced-scattering-coefficient images of a breast-like image.



**Fig. 8** The contrast-and-size map of resolution by using CNR values as gray-level intensities for the reconstructed absorption-coefficient images of an MRI breast image.

with less exception, indicating a regular tendency is shown. Moreover, from a detailed inspection in the example, no cross-talk exists in  $\mu_a$  or  $\mu'_s$  maps for a complicated composition.

Likewise, the visible differences among these submaps are hard to observe; thus, an alternative evaluation is nontrivial. The CSD resolution approach was applied for advanced analysis as shown in Sec. 4.4.

Following the above discussion, a further comparison can be made between Figs. 6 and 7 and Figs. 8 and 9 as follows. Concerning the influence of the cross-talk, it seems to appear in the case of the phantom with a high-contrast inclusion rather than a low-contrast inclusion. From the view point of the CNR values and the cross-talk, the inclusion in a complicated cross-section (e.g., an MRI breast image) is not simple to be detected but has little cross-talk for a same contrast of inclusion to background when compared with a simple one (e.g., a breast-like image), indicating that cross-talk effects might be ignored for detecting a real tumor *in vivo*.

### 4.3 Evaluation of the Application to a Homogenous Background Image with a Single Inclusion

For a detailed and numerical evaluation, CNR as a measure and the approach to plot a CSD resolution curve were used for evaluation on the above examples. Owing to slight differentiation, we simply depict two source-and-detector

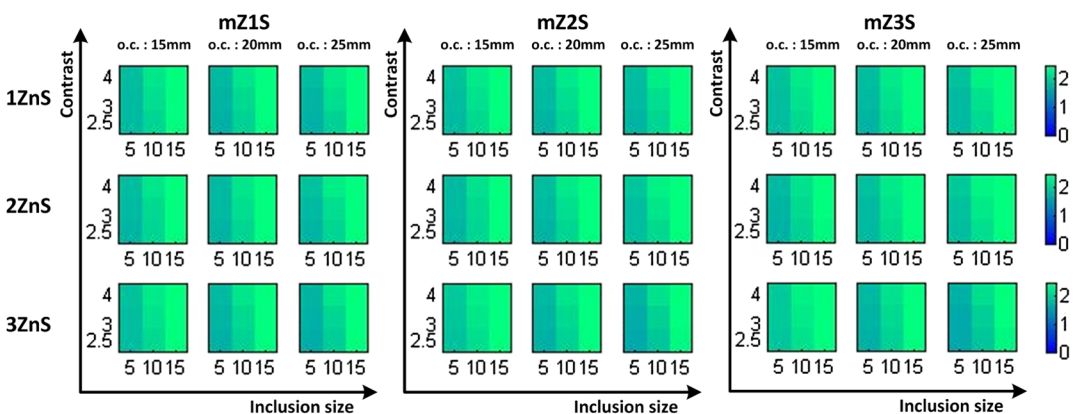
arrangements, respectively, with maximum and minimum values. According to the approach, Figs. 10 to 13 corresponding to Figs. 6 to 9 are explained as follows.

Related to  $\mu_a$  and  $\mu'_s$  images of a breast-like image, Figs. 10 and 11 show CSD resolution curves for varied off-centered distances of inclusion; further, the upper and lower rows were obtained based on inclusion sizes and contrasts, correspondingly. As shown in Figs. 10 or 11, the difference between the maximum and minimum values is small; the values in contrast in the lower row show a larger difference than the values in size in the upper row. Compared with the CNR values of  $\mu'_s$  images in Fig. 11, CNR values of  $\mu_a$  images in Fig. 10 have less separation, representing that the reconstruction of the absorption images is more difficult than the reduced-scattering ones.

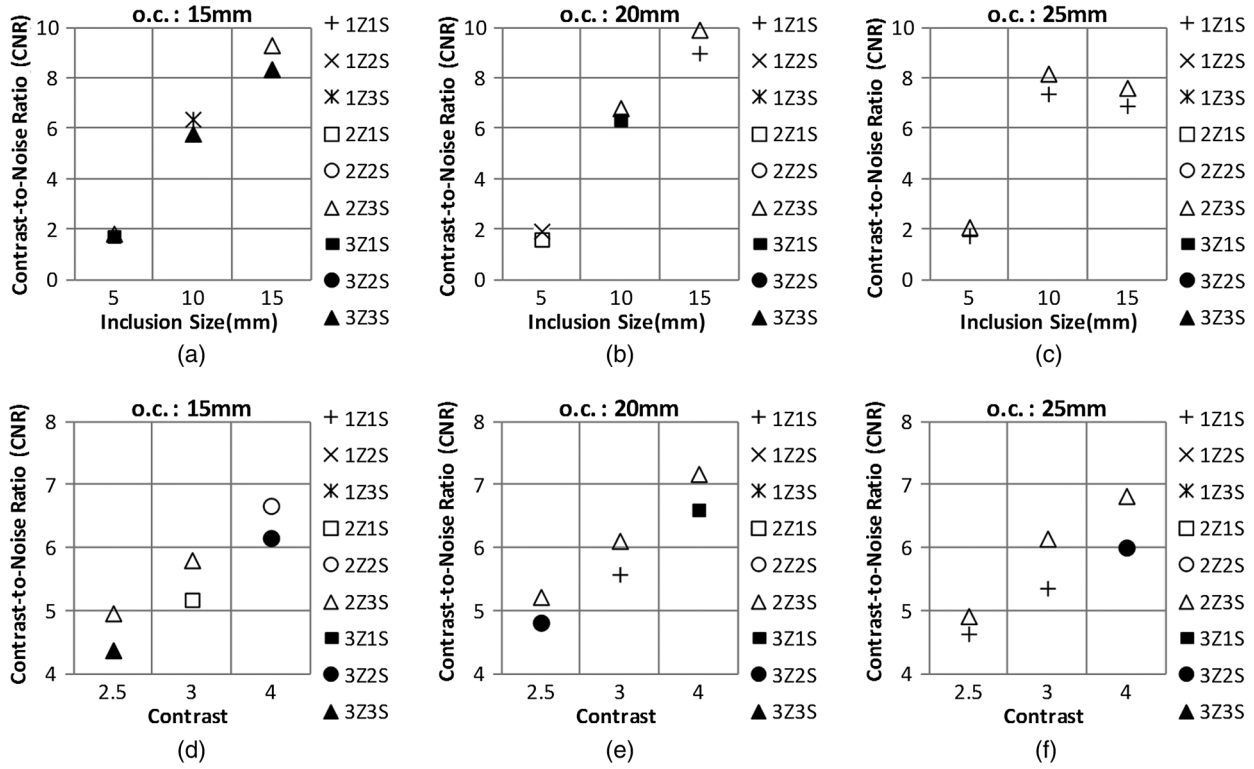
Moreover, both from Figs. 10 and 11, it is noted that a quite frequent hollow triangle  $\Delta$  appears indicating that 2Z3S source-and-detector arrangement yields apparently high CNR values superior to the other eight configurations.

### 4.4 Evaluation of the Application to an MRI Breast Image with a Single Inclusion

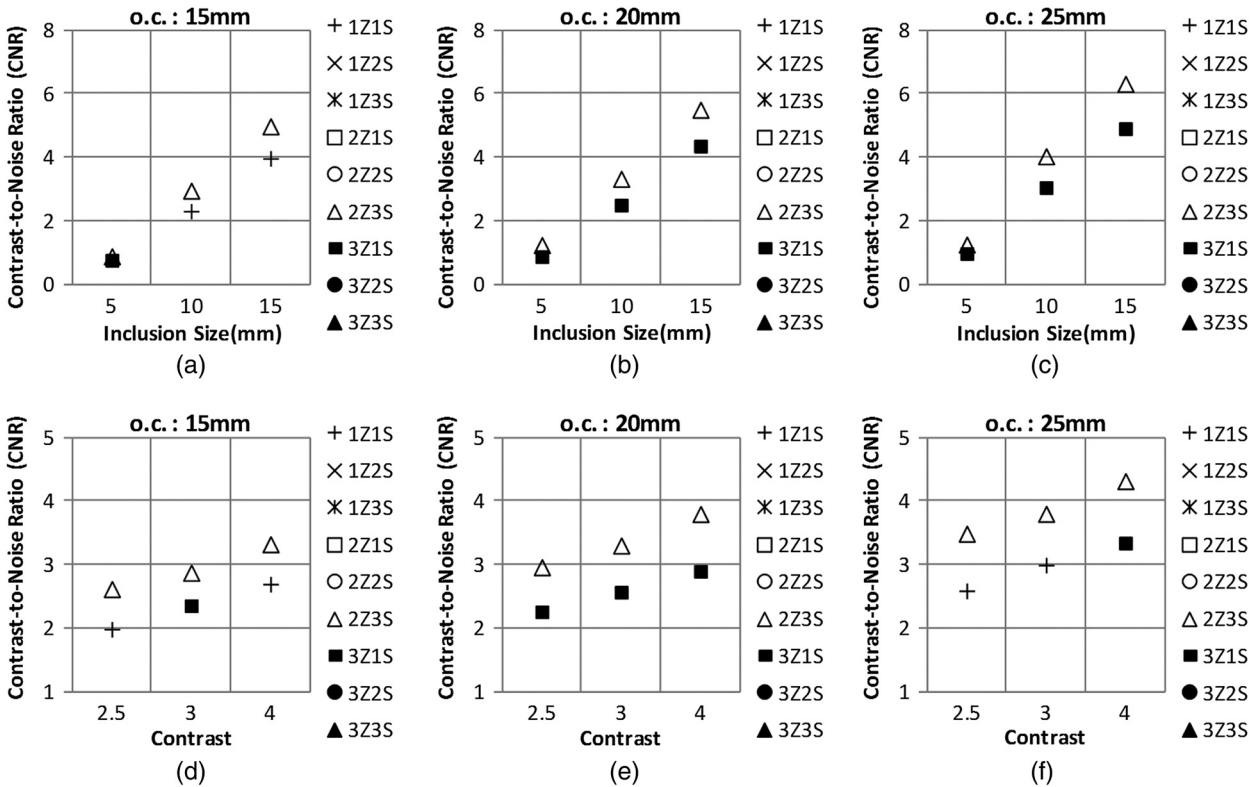
In this subsection, evaluation was made for an MRI breast image and the CSD resolution curves of  $\mu_a$  and  $\mu'_s$  images are shown in Figs. 12 and 13. For a realistic breast image, the differentiation based on inclusion sizes is near



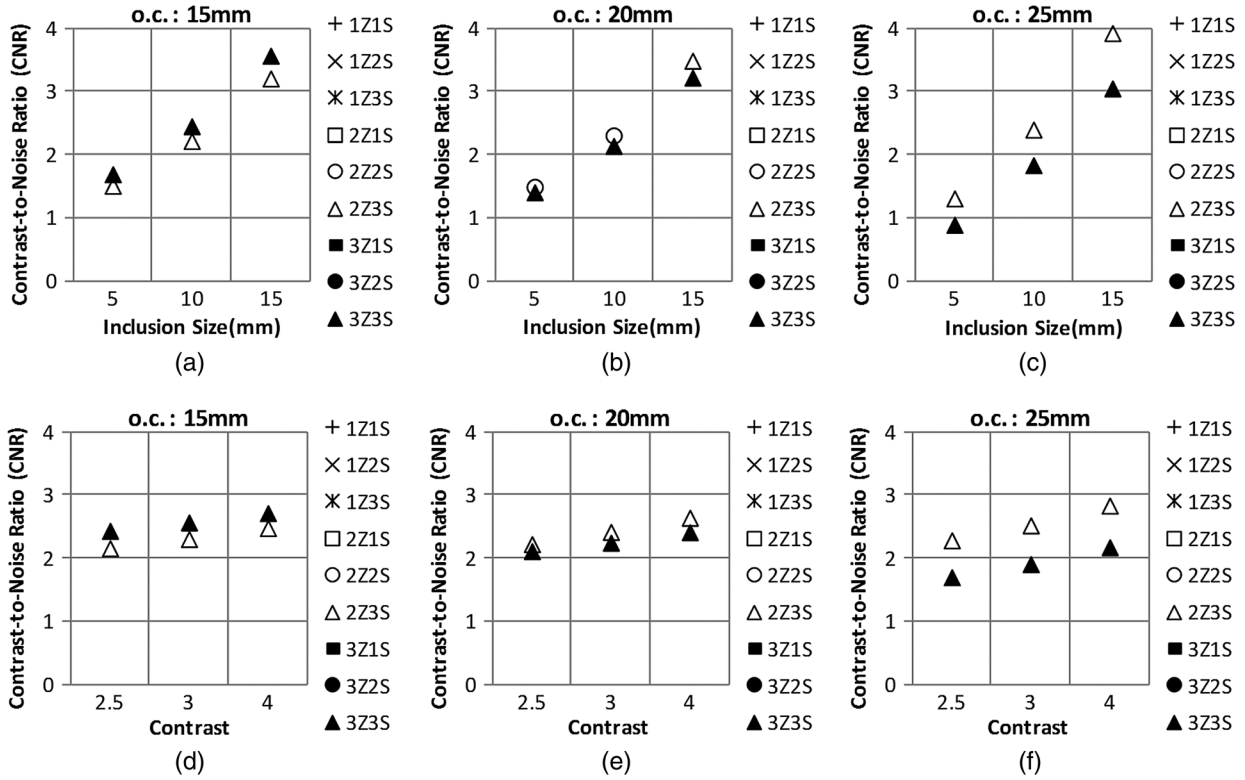
**Fig. 9** The contrast-and-size map of resolution by using CNR values as gray-level intensities for the reconstructed reduced-scattering-coefficient images of an MRI breast image.



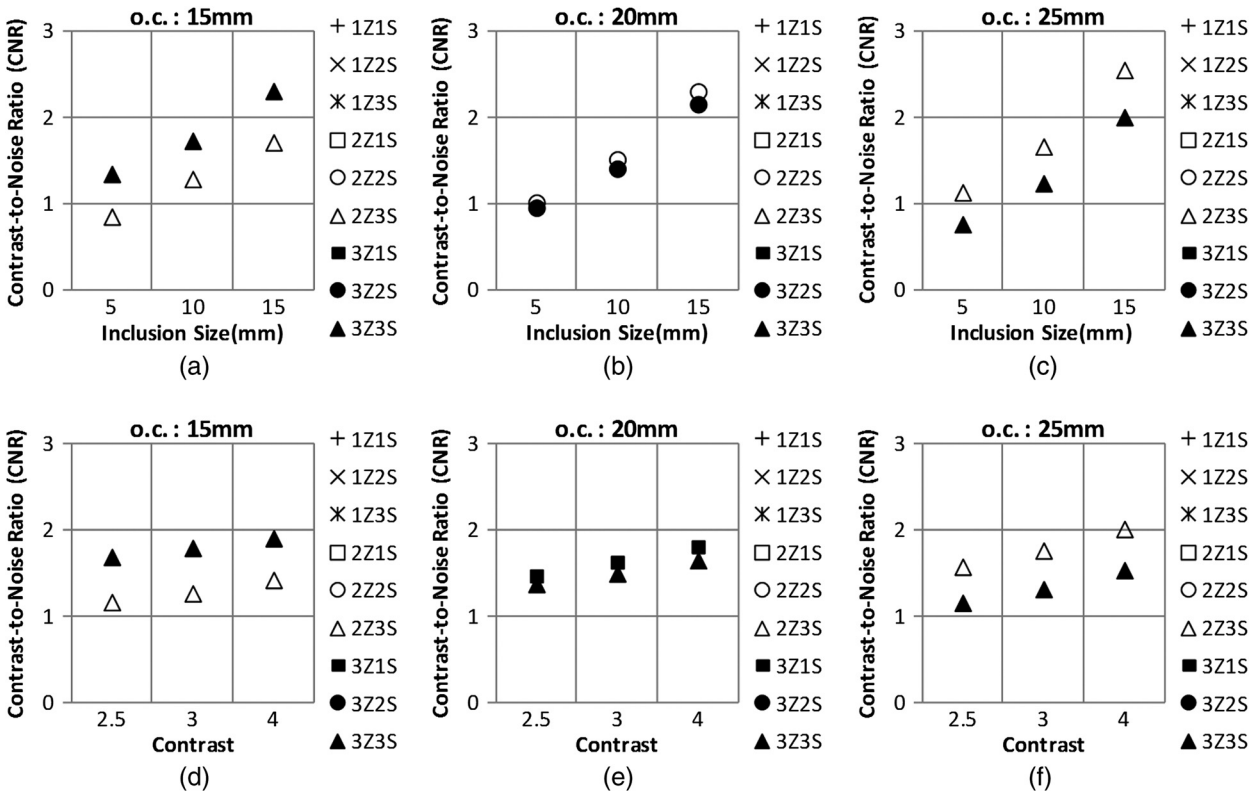
**Fig. 10** The CSD resolution curve plotted from calculating the average value of the projection corresponding to the axis (size or contrast) in Fig. 6. (a) to (c) and (d) to (f) are the CSD resolution curves corresponding to the size and contrast, respectively, for  $\mu_a$  images of a breast-like image.



**Fig. 11** The CSD resolution curve plotted from calculating the average value of the projection corresponding to the axis (size or contrast) in Fig. 7. (a) to (c) and (d) to (f) are the CSD resolution curves corresponding to the size and contrast, respectively, for  $\mu_s$  images of a breast-like image.



**Fig. 12** The CSD resolution curve plotted from calculating the average value of the projection corresponding to the axis (size or contrast) in Fig. 8. (a) to (c) and (d) to (f) are the CSD resolution curves corresponding to the size and contrast, respectively, for  $\mu_a$  images of an MRI breast image.



**Fig. 13** The CSD resolution curve plotted from calculating the average value of the projection corresponding to the axis (size or contrast) in Fig. 9. (a) to (c) and (d) to (f) are the CSD resolution curves corresponding to the size and contrast, respectively, for  $\mu_s$  images of an MRI breast image.

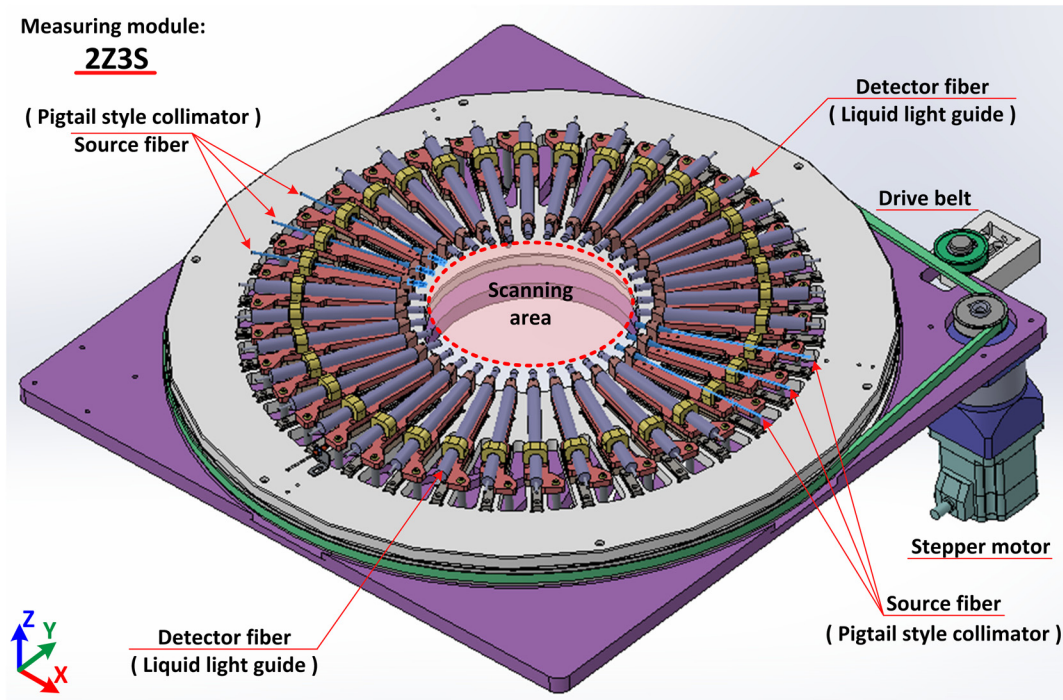


Fig. 14 The design diagram for the 2Z3S configuration.

to that of contrasts either in the  $\mu_a$  or  $\mu_s'$  image. As shown in Figs. 12 and 13, CNR differentiation between source-and-detector arrangements is difficult to observe, but 3Z3S ( $\blacktriangle$ ) and 2Z3S ( $\triangle$ ) are much more preferred because of their higher CNR values. Apparently, 3Z3S source-and-detector arrangement performs well for an inclusion embedded near the center, while 2Z3S is good for an inclusion near the boundary.

From our experience, the difference among the qualities of the reconstructed images is insignificant as the source-and-detector combination is beyond an optimal number. Based on the consideration of effectiveness and efficiency, 3Z3S arrangement has an advantage in efficiency and takes several seconds for a complete scanning, while 2Z3S needs around 10 s therefore both scanning times are acceptable; therefore, either 3Z3S or 2Z3S arrangement can be adopted in practice where one design diagram is shown in Fig. 14.

From the above examples, it can be concluded that CSD resolution curve corresponding to the contrast, i.e., the lower rows in Fig. 12 or 13, is chosen for investigation and evaluation owing to the visible difference when compared with the curves on size. For finding the tumor, moreover, the tumor contrast is a more important characteristic than its size; thus, the summation of CNR values for varied sizes, i.e., the projection on the contrast, is adopted rather than the summation for varied contrasts.

## 5 Conclusion

In this paper, we have demonstrated the design of varied source-and-detector arrangements in the ring-scanning mechanism for our NIR DOT imaging system in the FD. In this study, a series of forward and inverse simulations has been completed for each case shown in Fig. 5, where we have chosen a physiologically relevant contrast in a

tumor-sized inclusion. In our measuring system of DOI, the scanning angle was assumed to be multiples of 10 deg; alternatively, it can be predefined by the user for further requirement on scanning time or resolution. In general, increasing the number of measurements improves the quality of the reconstructed images and the image accuracy. Obviously, the design proposed here is much more robust than other fixed source-and-detector systems. Prior to the construction of the measuring system, the evaluation is vital; however, determining the optimal source-and-detector arrangements is not a simple task between effectiveness and efficiency for clinical diagnosis. According to our experience, the quality of the reconstructed optical-property images can be improved with advanced image reconstruction algorithms, such as interprocessing with high-pass filtering,<sup>32</sup> edge-preserving regularization algorithm,<sup>33</sup> and so on. Therefore, the efficiency becomes the main point to be considered beyond an acceptable image resolution. As shown in the results and evaluation, the 2Z3S or 3Z3S configuration is the optimal design for the ring-scanning mechanism based on the resolution of reconstructed optical-property images and the scanning time of mechanism.

## Acknowledgments

This research was sponsored by the National Science Council through grants NSC 101-2221-E-008-010-MY2, NSC 101-2221-E-008-093-MY3, and NSC 101-2221-E-236-014.

## References

1. P. J. Cassidy and G. K. Radda, "Review: molecular imaging perspectives," *J. R. Soc. Interface* **2**(3), 133–144 (2005).
2. F. C. Flack, "Recent advances in medical functional imaging," *Eng. Sci., and Edu. J.* **3**(5), 213–222 (1994).
3. A. Hielscher et al., "Near-infrared diffuse optical tomography," *Dis. Markers* **18**(5–6), 313–337 (2002).

4. B. W. Pogue et al., "Comparison of imaging geometries for diffuse optical tomography of tissue," *Opt. Express* **4**(8), 270–286 (1999).
5. B. W. Pogue et al., "Instrumentation and design of a frequency domain diffuse optical tomography imager for breast cancer detection," *Opt. Express* **1**(13), 391–403 (1997).
6. F. E. W. Schmidt et al., "A 32-channel time-resolved instrument for medical optical tomography," *Am. Inst. Phys.* **71**(1), 256–265 (2000).
7. B. W. Pogue et al., "Quantitative hemoglobin tomography with diffuse near-infrared spectroscopy: pilot results in the breast," *Radiology* **218**(1), 261–266 (2001).
8. T. O. McBride et al., "Multispectral near-infrared tomography: a case study in compensating for water and lipid content in hemoglobin near-imaging of the breast," *J. Biomed. Opt.* **7**(1), 72–79 (2002).
9. S. Jiang et al., "Quantitative analysis of near-infrared tomography: sensitivity to the tissue-simulating precalibration phantom," *J. Biomed. Opt.* **8**(2), 308–315 (2003).
10. N. Ifimia et al., "A compact, parallel-detection diffuse optical mammography system," *Rev. Sci. Instr.* **74**(5), 2834–2842 (2003).
11. T. Yates et al., "Optical tomography of the breast using a multi-channel time-resolved imager," *Phys. Med. Biol.* **50**(11), 2503–2517 (2005).
12. G. Gulsen et al., "Design and implementation of a multifrequency near-infrared diffuse optical tomography system," *J. Biomed. Opt.* **11**(1), 140020 (2006).
13. G. Gulsen et al., "Combined diffuse optical tomography (DOT) and MRI system for cancer imaging in small animals," *Tech. Canc. Res. Treat.* **5**(4), 351–364 (2006).
14. J. Wang et al., "Near-infrared tomography of breast cancer hemoglobin, water, lipid, and scattering using combined frequency domain and cw measurement," *Opt. Lett.* **35**(1), 82–84 (2010).
15. X. Li et al., "Integrated diffuse optical tomography and photoacoustic tomography: phantom validations," *Biomed. Opt. Express* **2**(8), 2348–2353 (2011).
16. S. B. Colak et al., "Tomographic image reconstruction from optical projections in light-diffusing media," *Appl. Opt.* **36**(1), 180–213 (1997).
17. B. Kanmani and R. M. Vasu, "Diffuse optical tomography through solving a system of quadratic equations: theory and simulations," *Phys. Med. Biol.* **51**(4), 981–998 (2006).
18. B. Alacam et al., "Pharmacokinetic-rate images of indocyanine green for breast tumors using near-infrared optical methods," *Phys. Med. Biol.* **53**(4), 837–859 (2008).
19. R. Padmaram, "The overall instrument design," Chapter 3 in *Design, Fabrication, and Testing of a Versatile, and Low-Cost Diffuse Optical Tomographic Imaging System*, MD Thesis, pp. 30–65, IISc, Bangalore, India (2007).
20. S. B. Colak et al., "Clinical optical tomography and NIR spectroscopy for breast cancer detection," *IEEE J. Sel. Top. Quant.* **5**(4), 1143–1158 (1999).
21. T. D. Yates et al., "Time-resolved optical mammography using a liquid coupled interface," *J. Biomed. Opt.* **10**(5), 054011 (2005).
22. S. M. W. Y. van de Ven et al., "Optical imaging of the breast," *J. Canc. Imaging* **8**(1), 206–215 (2008).
23. R. Al abdi et al., "Optomechanical imaging system for breast cancer detection," *J. Opt. Soc. Am. A* **28**(12), 2473–2493 (2011).
24. M. L. Flexman et al., "Digital optical tomography system for dynamic breast imaging," *J. Biomed. Opt.* **16**(7), 076014 (2011).
25. K. D. Paulsen and H. Jiang, "Spatially varying optical property reconstruction using a finite element diffusion equation approximation," *Med. Phys.* **22**(6), 691–701 (1995).
26. P. F. Judy et al., "Contrast-detail curves for liver CT," *Med. Phys.* **19**(5), 1167–1174 (1992).
27. B. W. Pogue et al., "Image analysis methods for diffuse optical tomography," *J. Biomed. Opt.* **11**(3), 033001 (2006).
28. S. Rivetti et al., "Comparison of different computed radiography systems: physical characterization and contrast detail analysis," *Med. Phys.* **37**(2), 440–448 (2010).

29. W. J. H. Veldkamp et al., "Contrast-detail evaluation and dose assessment of eight digital chest radiography," *Eur. Radiol.* **16**(2), 333–341 (2006).
30. X. Song et al., "Automated region detection based on the contrast-to-noise ratio in near-infrared tomography," *Appl. Opt.* **43**(5), 1053–1062 (2004).
31. L. Y. Chen, M.-C. Pan, and M.-C. Pan, "Visualized numerical assessment for near infra-red diffuse optical tomography with contrast-and-size detail analysis," *Opt. Rev.* **20**(1), 19–25 (2013).
32. M.-C. Pan et al., "Highly resolved diffuse optical tomography: a systematic approach using high-pass filtering for value-preserved images," *J. Biomed. Opt.* **13**(2), 024022 (2008).
33. L. Y. Chen, M.-C. Pan, and M.-C. Pan, "Implementation of edge-preserving regularization for frequency-domain diffuse optical tomography," *Appl. Opt.* **51**(1), 43–54 (2012).



**Jhao-Ming Yu** received his MS degrees in mechanical and electro-mechanical engineering from National Formosa University, Taiwan, in 2009. He is currently pursuing his PhD study at the Department of Mechanical Engineering, National Central University. His research interests include various aspects of diffuse optical tomography, opto-mechatronics design, and illumination optical design.



**Min-Cheng Pan** received his BEng and MS degrees from National Chiao Tung University and National Taiwan University in 1988 and 1990, respectively, and his PhD degree from the Applied Optics Group of Department of Physics, University of Reading, England, in 1999. He is currently a professor in the Department of Electronic Engineering, Tunghnan University in Taiwan. His research interests include image restoration/super-resolution, image reconstruction, numerical method, electronic circuits and medical imaging systems, light-emitting diode lighting design, and interdisciplinary research.



**Min-Chun Pan** received his PhD degree in mechanical engineering from the Katholieke Universiteit Leuven, Belgium, in May 1996. In 1996, he was a senior researcher at the Sanyang Industry Corporation, and, meanwhile, a junction associate professor at the Department of Forensic Science, Central Police University, Taiwan. After a two-and-half-year career in the industry, in 1999, he joined the Department of Mechanical Engineering at the National Central University as an assistant professor. He has been an associate professor and full professor with both the Mechanical Engineering Department and the Graduate Institute of Biomedical Engineering since 2003 and 2007, respectively. His research interests are in the areas of biomedical signal processing, sensing technology, and machine fault diagnostics, etc.